# Impact of Graphene Edges on Enhancing the Performance of Electrochemical Double Layer Capacitors

Alexander J. Pak, Eunsu Paek, and Gyeong S. Hwang*

Department of Chemical Engineering, University of Texas, Austin, Texas 78712, United States

S *Supporting Information*

ABSTRACT: The inherently large surface area and electrical conductivity of graphene-like electrodes have motivated extensive research for their use in supercapacitors. Although these properties are beneficial for the electric double layer (EDL) capacitance, the full utilization of graphene is curtailed by its intrinsically limited quantum capacitance due to the low density of electronic states near the neutrality point. While recent work has demonstrated that modifications to graphene can generally mitigate this limitation, a comprehensive analysis of the impact of graphene edges, which can be created during synthesis and post-treatment, has yet to be reported. Using a theoretical approach, we investigate the influence of graphene edges on both the quantum and EDL capacitances using edge-passivated zigzag graphene nanoribbons (ZGNRs) in [BMIM][PF$_6$] ionic liquid as model systems. Our findings show that the presence of edges improves the quantum capacitance by increasing the electronic density of states, which is further amplified as the ZGNR width decreases. Our analysis also reveals that the EDL microstructure can be noticeably altered by the edges, which in turn increases the EDL capacitance. Through comparisons with pristine graphene electrodes, our study clearly highlights that edge defects in graphene-like electrodes can enhance supercapacitor performance by dramatically augmenting both EDL and quantum capacitances.
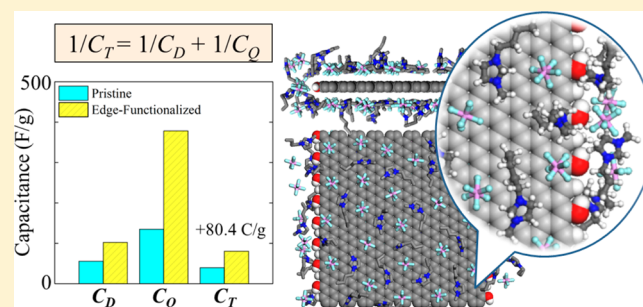
INTRODUCTION

The growing demand for high-power applications such as electric vehicles, load-leveling, communications, and portable electronics has stimulated research into improved electrochemical energy storage technologies.[1,2] Of these, electrochemical double layer capacitors (EDLCs or supercapacitors) have gained considerable interest due to their high specific power density and long cycle life.[3,4] To effectively implement EDLCs, however, their specific energy storage capabilities require further improvement.

To date, many efforts have explored the possible utilization of sp^2-based carbon nanomaterials, such as graphene, as electrodes owing to their large specific surface areas and good electrical conductivities.[5] These reports demonstrated noteworthy improvements in capacitance, which have been ascribed to several factors including greater electrode wetting/accessibility, improved electrical conductivity, and possible pseudocapacitance.[6−15] However, to develop strategies for increased performance, it is critical to understand the underlying molecular mechanisms at the electrode−electrolyte interface.

A recent series of experimental[16,17] and theoretical[18] studies involving interfaces near graphene-like electrodes were conducted in an effort to elucidate this fundamental behavior. The principal insight from these studies was that the total interfacial capacitance (C_T) is strongly dependent on the contributions of both the quantum (C_Q) and double layer (C_D)

capacitances which are in series. As a corollary, it was also shown that pristine graphene electrodes have intrinsically limited C_Q near the charge neutrality point, which subsequently curtailed C_T. But several computational results have since reported that structural[19−22] or chemical[23] modification of graphene-like electrodes can significantly improve C_Q.

In these previous studies, it is worth mentioning that the scope was limited to phenomena near the basal plane of graphene where ion accumulation mostly occurs, which has traditionally been the structural region of interest. But given the recently revealed sensitivity of C_T to C_Q and C_D, it would be valuable to explore similar phenomena near the edges of graphene for several reasons. First, it is well-known that the presence of edges can alter the electronic structure of graphene, which has been successfully utilized in many electrochemical applications.[24−26] Such modifications to the electronic structure may subsequently affect C_Q. It is also possible that the electric double layer (EDL) microstructure, and therefore C_D, can be noticeably perturbed near the edge sites, similarly to the case of prismatic graphite electrodes with different degrees of corrugation.[27,28] Furthermore, research into potential applications for graphene edges seems timely given recent advances in the fabrication of high-quality graphene edges.[29] One example

of this is a recent demonstration by Zhang et al. in which the splitting of vertically aligned carbon nanotubes into graphene nanoribbons exhibited a 4-fold increase in specific capacitance.[30] However, to the best of our knowledge, a fundamental study on the impact of edge defects on both C_Q and C_D has never been reported.

In this work, we investigate the effect of edge defects on C_T using edge-passivated graphene nanoribbons (GNRs) as model systems; we consider only zigzag GNRs (ZGNRs) since they can be metallic and neglect armchair GNRs which are always semiconducting. Our strategy is to decouple the relative impacts on C_Q and C_D using a first-principles-based computational approach. First, we employ density functional theory (DFT) to study the electronic structure and C_Q of two types of edge-passivated ZGNRs at varying widths. Using classical molecular dynamics (MD), we then study the microstructure and C_D of a ZGNR immersed in $[BMIM][PF_6]$, an ionic liquid which is an advantageous class of electrolyte given its large electrochemical window, low volatility, nonflammability, and high thermal and chemical stability.[31,32] Our study clearly demonstrates that the presence of edges can have a positive influence on both C_Q and C_D when compared to the case of pristine graphene and therefore enhances the overall C_T.

■ COMPUTATIONAL METHODS

Density Functional Theory Calculations. The atomic and electronic structures of each investigated ZGNR were calculated using DFT within the spin-polarized Perdew–Wang 91 generalized gradient approximation (GGA-PW91),[33] as implemented in the Vienna Ab initio Simulation Package[34] (VASP); the Vosko–Wilk–Nusair interpolation method was used for the correlation part of the exchange correlation functional.[35] We used the projector augmented wave (PAW) method to describe the interaction between ion core and valence electrons[36] and a plane-wave basis set with a kinetic energy cutoff of 400 eV.

We first investigated two different types of edge-passivated ZGNRs at two different widths: (i) single hydrogen (H) termination (herein called H-18ZGNR and H-60ZGNR) and (ii) alternating termination by a hydroxyl (OH) and single H (herein called OH-18ZGNR and OH-60ZGNR). The OH moiety is considered one of the most stable oxidation groups and is known to prefer orienting parallel to the plane of the GNR.[37,38] The ZGNRs were modeled using rectangular 2×9 (as shown in Figure 1) and 2×30 supercells (corresponding to 72 and 240 C atoms, respectively) with a GGA-optimized lattice constant of 2.466 Å. Periodic boundary conditions were employed in all three directions, but vacuum spaces of 10 and 20 Å were included in the z and y directions, respectively, to remove interactions with adjacent images (additional vacuum spacing does not noticeably affect our results as shown in Figure S1). For the Brillouin zone integration, we used a $6 \times 1 \times 1$ Monkhorst–Pack[39] mesh of k-points to determine the optimal geometries and total energies and increased the mesh size to $14 \times 1 \times 1$ for electronic structure calculations. To make comparisons to the pristine graphene case, we performed similar electronic structure calculations using a four-atom rectangular cell with dimensions of 4.272×2.466 Å^2; here, a $21 \times 21 \times 1$ k-point mesh was used for Brillouin zone sampling.

To study the atomic charge distribution of ZGNRs at different widths, we additionally modeled rectangular 2×5 and 2×13 supercells for both H-ZGNR and OH-ZGNR cases using the same lattice constant, vacuum spacing, and k-point
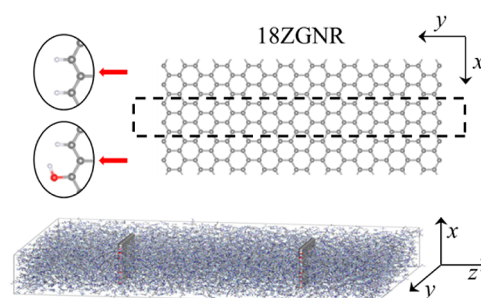

Figure 1. (top) Schematic of the zigzag graphene nanoribbon supercell (bound by the dashed lines) used in electronic structure calculations. The edges were passivated by either H or H/OH atoms where H and O are indicated by the white and red balls, respectively. (bottom) Schematic of the simulation box used in classical molecular dynamics simulations. The white, red, and gray balls indicate H, O, and C electrode atoms, respectively. The white, gray, and blue lines indicate the H, C, and N atoms in BMIM, while the pink and cyan lines indicate the P and F atoms in PF$_6$. Periodic boundary conditions were applied in all three directions.

mesh. The atomic charges were evaluated using grid-based Bader analysis[40] under neutral and charged (± 1 e per supercell) conditions; the latter case was used to study the excess charge redistribution. The calculated Bader charges for OH-18ZGNR were subsequently used in the MD calculations.

Molecular Dynamics Calculations. The microstructure of $[BMIM][PF_6]$ near OH-18ZGNR electrodes was studied from MD simulations based on the OPLS-AA force field[41,42] using the Large-Scale Atomic/Molecular Massively Parallel Simulator (LAMMPS) program.[43] As illustrated in Figure 1, the simulation consisted of 3036 pairs of $[BMIM][PF_6]$ surrounding two electrodes (39.46×39.2 Å^2) separated by 100 Å in both the y and z directions, which was large enough such that the electrolyte maintained a bulk density in the regions between electrodes. The inter- and intramolecular force field parameters for BMIM, PF$_6$, and graphitic C are described in ref 18. We used the generalized OPLS force field parameters for OH and H moieties.[41] During the simulations, the electrode atoms were fixed in position.

We studied when the excess surface charge density $\sigma = 0$, 80.4, and -80.4 C g^{-1} using the predicted atomic charges from Bader analysis. We ran each MD simulation initially at 1000 K for 1 ns followed by 1 ns at 300 K for three cycles to equilibrate the system using a time step of 1 fs. Production runs were carried out for 2 ns with atomic positions recorded every 5 ps. All runs were in the NVT ensemble with the temperature controlled by a Nosé–Hoover thermostat[44] with a 100 fs damping parameter. MD results reported herein were obtained from the average of five independent simulations with different initial atomic configurations. Further details about the MD simulations are described in ref 18.

■ RESULTS AND DISCUSSION

Electronic Structure and Quantum Capacitance. In this section, we present the band structures and density of states (DOS) of the investigated ZGNRs, considering both the antiferromagnetic (AF) and ferromagnetic (FM) spin states. On the basis of the electronic structure, we then predict and analyze the quantum capacitance (C_Q) of the ZGNRs.

Figure 2a shows the DOS for H-18ZGNR (left) and H-60ZGNR (right) in the AF state (the insets show the FM state). According to our GGA-PW91 calculations for H-
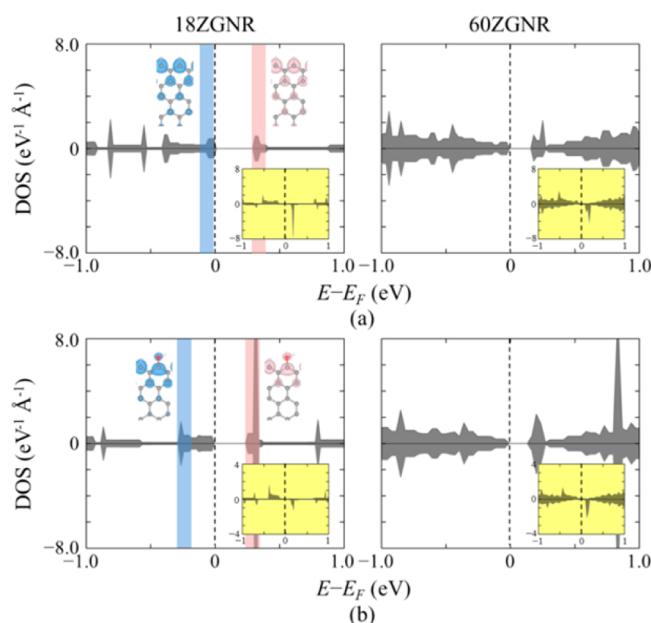
Figure 2. Spin-polarized total density of states (DOS) of (a) H-passivated and (b) alternating H-/OH-passivated zigzag graphene nanoribbons (ZGNR) at different widths in the antiferromagnetic state. The insets depict the corresponding DOS of the ferromagnetic state. Positive (negative) values of the DOS indicate the spin-majority (spin-minority) states. The Fermi level (E_F) is marked by the dashed line. The band-decomposed charge density isosurfaces (0.001 e bohr^{-3}) were obtained from the highlighted energy ranges.

18ZGNR, the AF state is marginally more stable ($\approx$0.6 meV Å^{-1}) than the FM state; other functionals including LDA ($\approx$0.2 meV Å^{-1}) and GGA-PBE ($\approx$1.0 meV Å^{-1}) predict similar results. In the AF case, a band gap of 0.30 eV is estimated to arise due to the differences in AF exchange interaction between sublattices.[38,45,46] In the FM case, the spin-majority and spin-minority states are both partially filled at the Fermi level (E_F). However, in the H-60ZGNR case, both the AF band gap (0.16 eV) and difference in energy between the AF and FM state ($\approx$0.0 meV Å^{-1}) are reduced, which is expected to occur as the GNR width increases.[45]

In both the AF and FM cases, the DOS exhibits peaks close to E_F (such as in the highlighted regions). It is well-known that these are primarily attributed to the quasi-localized p_z states at the edge sites,[37,38,45,46] which is also depicted by the band-decomposed charge density isosurfaces; H passivation removes the dangling sp^2 bonds that are characteristic of bare ZGNRs while the disrupted π bonds remain. Furthermore, these peaks tend to be more broadened in the H-60ZGNR case, which suggests that the degree of coupling between the edge p_z states and the π network increases as the ZGNR width increases.

Figure 2b shows the DOS for OH-18ZGNR (left) and OH-60ZGNR (right) in the AF state (the insets show the FM state). Similar to the H-18ZGNR case, the AF state of OH-18ZGNR is also marginally more stable ($\approx$0.4 meV Å^{-1}) than the FM state, although the addition of OH functional groups appears to reduce the spin order-induced stabilization. Consequently, the band gap in the AF state is reduced to 0.23 and 0.13 eV for OH-18ZGNR and OH-60ZGNR, respectively, while the FM state remains metallic. Comparing the OH-18ZGNR case to the H-18ZGNR case, we observe that in the former case the DOS peaks within $-0.5 < E - E_F < 0.5$ eV are narrowed toward E_F; the quasi-localized C p_z orbitals

tend to slightly overlap with the O 2p antibonding orbitals, as also seen in the band-decomposed charge density isosurfaces. However, the addition of OH in the 60ZGNR case does not noticeably affect the extent of localization, suggesting that the extent of coupling between the edge p_z states and π system is strong enough to be insensitive to the edge moieties when the ZGNR width is sufficiently large.

Using the procedure described in ref 18, we calculate the differential quantum capacitances ($C_{Q,diff} = d\sigma/d\phi_E$) for all four cases, where dσ and dϕ_E refer to the variations of excess surface charge density and local potential in the electrode, respectively. Since both the AF and FM states are likely to appear, the $C_{Q,diff}$ is computed from the average of the two cases. As shown in Figure 3, we then predict the integral C_Q ($= \sigma/\phi_E$ where $\sigma =$
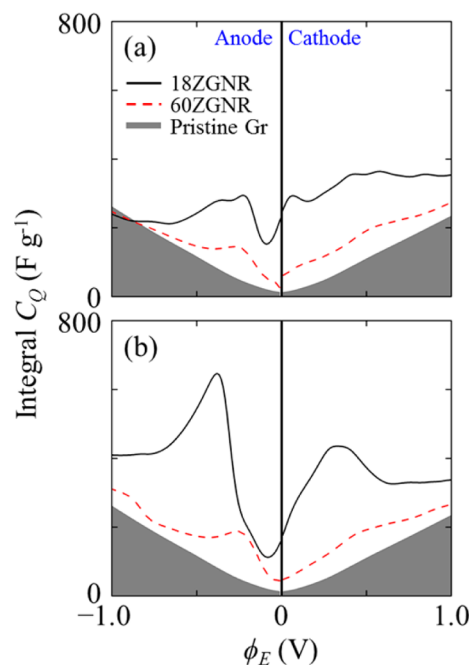

Figure 3. Integral quantum capacitances (C_Q) as a function of local electrode potential (ϕ_E) for the (a) H-passivated and (b) alternating H-/OH-passivated zigzag graphene nanoribbons (ZGNR) at different widths as compared to that of pristine graphene. The depicted C_Q of the ZGNR electrodes was computed from the average C_Q of the antiferromagnetic and ferromagnetic states. The middle line indicates the neutrality point.

$\int C_{Q,diff}\, d\phi_E$) which is the preferred metric to evaluate the total charge storage capability at a given ϕ_E. In comparison to the pristine graphene case, the C_Q of the ZGNRs tends to be increasingly enhanced as the ZGNR width decreases, which is especially apparent when $|\phi_E| < 0.5$ V (due to the additional availability of states). Our calculations further demonstrate that the addition of OH greatly improves C_Q in the 18ZGNR case but only marginally in the 60ZGNR case. We should also note that unlike pristine graphene electrodes, the ZGNR electrodes have intrinsically different C_Q profiles at the anode and cathode.

Beyond the C_Q, we also explore the local charge redistribution at the edges of ZGNRs at varying widths; the charge redistribution is particularly important as it can affect the electrostatic interactions at the electrode−electrolyte interface. To quantify this behavior, we use grid-based Bader analysis to compute the atomic charges.[40] In Figure 4a, we first present the atomic charges of the edge-passivating moieties of both H- and
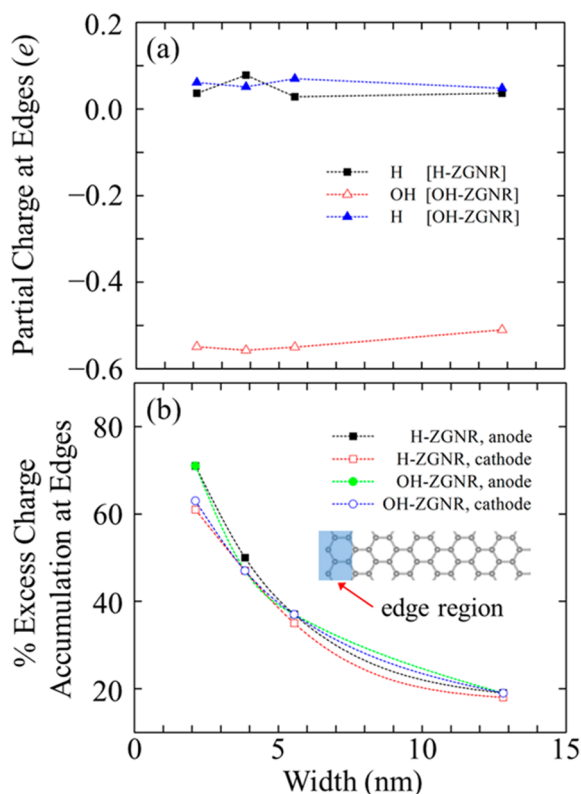
Figure 4. Estimated (a) partial charges of edge-passivating groups and (b) degree of excess charge accumulation at the edges of zigzag graphene nanoribbons (ZGNR) with varying width and edge passivation. The partial charges were computed from grid-based Bader analysis. The excess charge accumulation was calculated from the fractional amount of excess charge found at the edges (defined by the shaded region) after one charge carrier was injected into each ZGNR.

OH-ZGNRs. Here, the H and OH groups are expectedly positively and negatively charged, which will affect the microstructure of the interface as discussed below. Yet also note that the partial charges seem insensitive to the width of the ZGNR. We then estimate the degree of excess charge accumulation at the edges in Figure 4b; one electron or hole is injected into each system, after which the fraction of excess charge stored at the edges (defined up to a depth of 3.7 Å) is calculated. Both the H- and OH-ZGNR cases clearly demonstrate that the excess charge accumulation at the edges becomes more pronounced superlinearly as the GNR width becomes smaller. In the next section, we will discuss the implications of this behavior on the EDL microstructure and C_D.

Double Layer Microstructure and Capacitance. *Near Uncharged Electrodes.* We study the EDL microstructure and C_D of OH-18ZGNR immersed in [BMIM][PF$_6$] IL, which serves as a model system to understand how the presence of edges can affect the interfacial structure and C_D. We begin with a thorough analysis of the IL microstructure near uncharged electrodes. Figure 5a shows the two-dimensional (2D) mass density (ρ_m) profiles of BMIM (left) and PF$_6$ (right) when $\sigma = 0$ C g^{-1}. First, we draw attention to the ion segregation and ordering near the edges. The PF$_6$ profile exhibits distinct high-intensity (color range from yellow to dark red) spots directly above/below the edges whereas BMIM exhibits low-intensity shades (color range from purple to blue). This indicates that
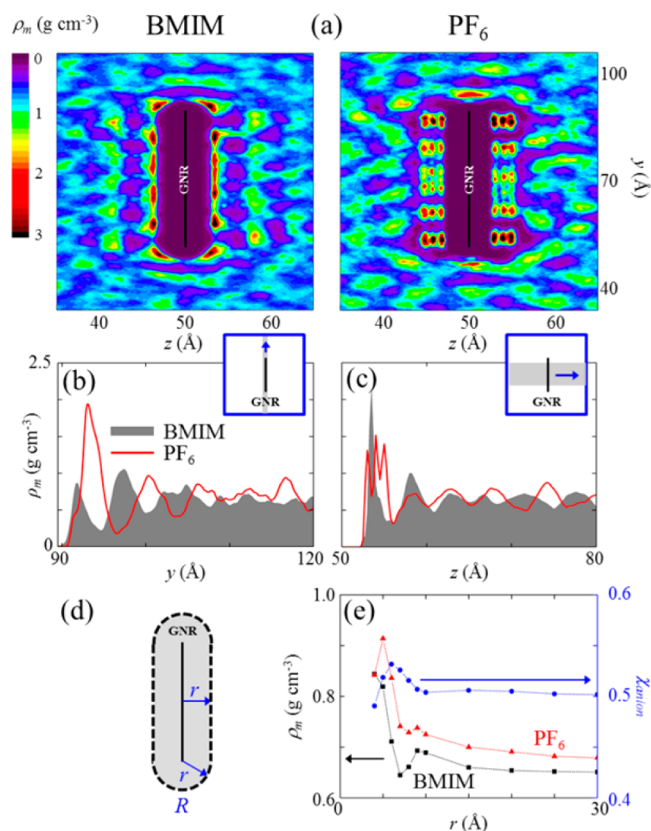

Figure 5. (a) Two-dimensional color map of mass density (ρ_m) profiles for BMIM and PF$_6$ near uncharged zigzag graphene nanoribbon electrodes alternatingly passivated by H and OH (OH-18ZGNR). The position of the electrode is indicated by the black line in the center of the color maps. (b) Average ρ_m along the edge direction (over the shaded region shown in the inset). (c) Average ρ_m along the basal plane (over the shaded region shown in the inset). (d) Schematic of region (R) used to calculate the average ρ_m surrounding the electrode as a function of distance (r). (e) Average ρ_m surrounding the electrode (left axis) and mixing parameter (χ_{anion}) of PF$_6$ (right axis).

PF$_6$ (BMIM) tends to be clustered (deficient) directly at the edge, which is primarily attributed to the strong electrostatic attraction (repulsion) between the PF$_6$ anion (BMIM cation) and the positively charged H atoms (see Figure S2 for the partial charges from Bader analysis). We also observe BMIM accumulation (PF$_6$ depletion) around the rims of the edges (adjacent to the negatively charged O atoms) and subsequent PF$_6$ accumulation (BMIM depletion) directly normal to the edge C atoms (which are positively charged). This alternating cascade of segregated anions and cations surrounding the edges results from the combined influence of electrostatic interactions between (i) anions/cations with the charged electrode atoms at the edges and (ii) IL ions with adjacent counterions. However, the degree of anion–cation segregation around the electrode tends to diminish near the basal region, as demonstrated by the mingled presence of high-intensity spots in both BMIM and PF$_6$ profiles. In Figure S3, we provide a snapshot of the IL ions adjacent to the electrode to visually demonstrate the decaying anion–cation cascade surrounding the electrode.

Next, we explore the variation in ρ_m as a function of distance from the electrode for BMIM and PF$_6$. The average ρ_m estimated along the edge direction (48 < z < 52 Å) (Figure 5b) shows a distinct (reduced) peak associated with PF$_6$

(BMIM) which can be expected based on Figure 5a. Interestingly, the ρ_m profiles reveal alternating layering of anions and cations. Such behavior is typical of ILs near charged surfaces,[47,48] indicating that the aforementioned charge redistribution toward the electrode edges is strong enough to trigger a similar response. In contrast, the average ρ_m estimated normal to the basal plane ($60 < y < 80$ Å) (Figure 5c) displays cation and anion profiles with spatial similarity (the ions maintain charge neutrality), which is consistent with previous studies near uncharged pristine graphene electrodes.[18,49−52] This suggests that although the basal plane is slightly positively charged due to the redistribution of electrons in the basal plane toward the edges ($\sigma_{basal} = 6.7$ C g^{-1} or 0.5 μC cm^{-2}), the electrostatic interactions are not significant enough to induce anion/cation segregation in the normal direction.

It would also be interesting to quantify the extent of PF$_6$ segregation from BMIM in order to evaluate the net ionic charge accumulation surrounding the electrode due to the presence of edges. We compute a mixing parameter (χ) which is calculated within the region (R) defined with radial extension r as shown in Figure 5d:

$$\chi = \frac{\int_R \rho_{m,anion}/MW_{anion} \, dR}{\int_R (\rho_{m,anion}/MW_{anion} + \rho_{m,cation}/MW_{cation}) \, dR} \quad (1)$$

where MW_i is the molecular weight of species i. The ρ_m averaged in R and χ_{anion} in R are presented in Figure 5e, which shows a maximum $\chi_{anion} = 0.53$ at $r = 6$ Å that quickly tapers to $\chi_{anion} \approx 0.50$ when $r > 10$ Å. In other words, charge neutrality is essentially maintained despite the slight amassment of PF$_6$ anions. This suggests that the presence of edges primarily influences the ordering and segregation of ions surrounding the electrodes while the net ionic charge accumulation is only marginally affected.

To determine the C_D from the microstructure, we first estimate the potential of zero charge (ϕ_Z) from the computed space charge variation (ρ_q) which is determined from the distribution of electrode and IL atoms with fixed atomic charges. We subsequently solve Poisson's equation ($\nabla^2 \phi = -\rho_q/\varepsilon_0$), in which ϕ is the potential variation and ε_0 is the vacuum permittivity (details are described in the Supporting Information). In Figure 6, the 2D ϕ profiles are depicted where the ϕ in the bulk IL region is taken as reference ($\phi = 0$ V). The

ϕ_Z, then, is determined from the average surface ϕ of the electrode, which we find to be 0.22 V; note that $\phi_Z > 0$ V is consistent with the observed accumulation of PF$_6$ anions. For comparison, pristine graphene (at $\sigma_{basal} = 6.7$ C g^{-1}) is estimated to have a similar potential drop of 0.19 V (with $\phi_Z \approx 0$ V).[53]

Near Charged Electrodes. Our analysis now extends to the case when the electrodes are charged. Figure 7a−d shows ρ_m

Figure 7. Mass density (ρ_m) profiles for BMIM and PF$_6$ near charged zigzag graphene nanoribbon electrodes alternatingly passivated by H and OH (OH-18ZGNR). (a−d) Two-dimensional color map of ρ_m for BMIM and PF$_6$ (the electrode position is indicated by the black line). (e, f) Average ρ_m along the basal plane (over the shaded region shown in the right panel). (g, h) Average ρ_m along the edge direction (over the shaded region shown in the right panel). (i, j) Average ρ_m surrounding the electrode and mixing parameter $\chi_{counterion}$) of the counterion as a function of distance (r) within the shaded region (R) shown in the right panel.

near OH-18ZGNR electrodes when $\sigma = \pm 80.4$ C g^{-1} (± 6.2 μC cm^{-2}). Near the edges of both the cathode and anode, the profiles of each counterion (co-ion) increase (decrease) in both intensity and distinction as compared to the neutral case. This suggests that the alternating cascade of anions/cations surrounding the edges exhibits greater ion segregation than the uncharged case, which is expected since the majority fraction of injected charge carriers accumulate at the edges and thereby enhance the electrostatic attraction (repulsion) with counterions (co-ions). Furthermore, the alternating cascade
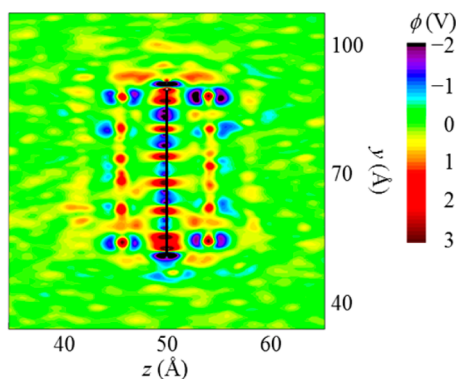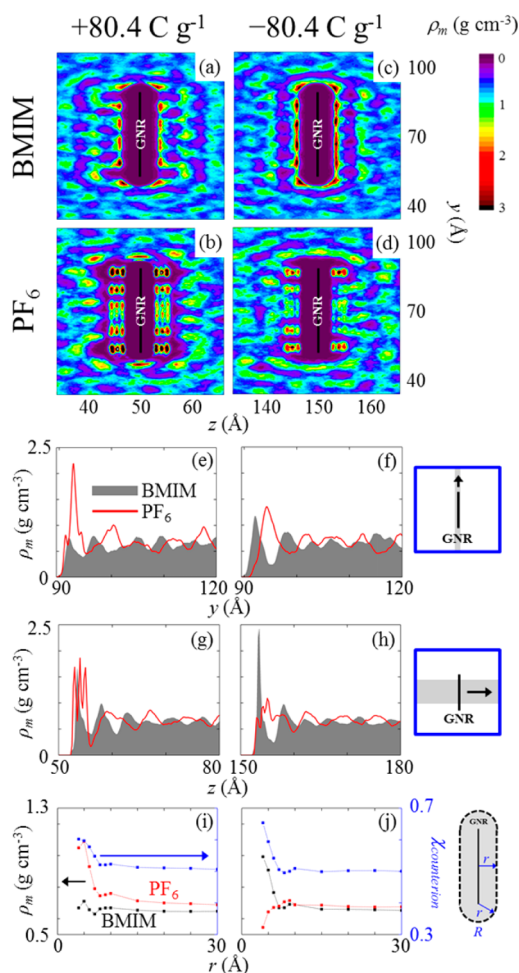
Figure 6. Two-dimensional color map of the potential (ϕ) profile near uncharged zigzag graphene nanoribbon electrodes alternatingly passivated by H and OH (OH-18ZGNR). The position of the electrode is indicated by the black line in the color map. The ϕ in the bulk region of the electrolyte is taken as reference ($\phi = 0$ V).

21774

dx.doi.org/10.1021/jp504458z | J. Phys. Chem. C 2014, 118, 21770−21777

seems to extend further into the basal plane region when the electrode is positively charged rather than negatively charged. We postulate that this behavior manifests more strongly near the cathode since PF_6 anions are more compact and symmetric than BMIM cations, which therefore facilitates the layering along the electrode width.

We next examine the variation in ρ_m along the edge direction and normal to the basal plane. Figure 7e,f depicts the average ρ_m in the edge direction near the cathode and anode, respectively. Here, the first peak in the PF_6 profile is noticeably enhanced (diminished) at the cathode (anode) edge. The first peak in the BMIM profile, on the other hand, is only marginally suppressed (augmented) at the cathode (anode) edge. In addition, the alternating layering behavior, as also seen in the uncharged case (Figure 5b), is maintained (suppressed) at the cathode (anode) edge. These observations suggest that the electrostatic interaction with the positively charged H atom still tends to dominate ion accumulation and segregation behavior directly at the edges since the injected charge carriers merely strengthen (reduce) the partial charge of H at the cathode (anode). In direct contrast, the average ρ_m profiles near the basal plane (Figure 7g,h) do not display distinct alternation between PF_6 and BMIM peaks, indicating that the ions are less noticeably segregated in the direction normal to the basal plane. In other words, the electrostatic interactions from the basal plane ($\sigma_{basal} \approx \pm 54.1$ C g^{-1}) are not strong enough to induce such layering behavior.

To quantify the overall counterion accumulation surrounding the electrode, we calculate $\chi_{counterion}$ and the corresponding R-averaged ρ_m profiles near the cathode and anode in Figure 7i,j. Although it is readily apparent that the average ρ_m of counterions near the cathode tends to exceed that of the anode when $r < 6$ Å, the net ratio of counterions to co-ions remains similar for both cathode and anode. Therefore, the overall charge stored at the electrode−electrolyte interface is expected to be comparable near the cathode and anode, despite differences in the edge-induced perturbations to their respective microstructures.

Figure 8 shows the predicted 2D ϕ profiles near the charged OH-18ZGNR electrodes. Using the same approach from the
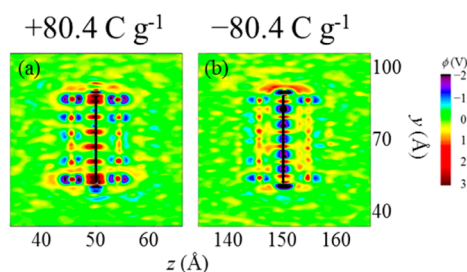

Figure 8. Two-dimensional color map of potential (ϕ) profiles near charged zigzag graphene nanoribbon electrodes alternatingly passivated by H and OH (OH-18ZGNR). The position of the electrode is indicated by the black line. The ϕ in the bulk region of the electrolyte is taken as reference ($\phi = 0$ V).

uncharged case, we estimated the average surface ϕ. Then taking the difference between the surface ϕ and ϕ_Z, we find that the potential drop in the EDL (ϕ_D) is 0.79 and −0.78 V for the cathode and anode, respectively. For comparison, the respective ϕ_D at $\sigma = \pm 80.4$ C g^{-1} in the pristine graphene case are 1.45 and −1.38 V.[53] The reduction in ϕ_D should be unsurprising since most of the excess charge accumulates at the edges where it can be easily screened, thereby lowering the overall overscreening of counterions near the majority of the electrode. Correspondingly, the integral C_D using the OH-18ZGNR electrodes is 101.8 (103.1) F g^{-1} when $\sigma = 80.4$ (−80.4) C g^{-1}, which is nearly a factor of 2 greater than that of the respective C_D using pristine graphene.[53] Given that the excess charge accumulation at the edges increases with the narrowing of the ZGNR, we may also expect the enhancement in C_D to increase in turn.

Edge Effects on the Total Interfacial Capacitance. As summarized in Table 1, we have predicted the C_T and the applied potential (ϕ_a) when $\sigma = \pm 80.4$ C g^{-1} using OH-18ZGNR electrodes based on the combination of the integral C_Q and C_D ($1/C_T = 1/C_Q + 1/C_D$). We find that C_T is 80.2 (76.8) F g^{-1} at the cathode (anode), which is nearly twice that of the predicted C_T near pristine graphene.[53] Based on our analysis of C_Q and C_D, it is clear that this enhancement can be attributed to significant gains in both C_Q and C_D. We therefore anticipate that the nanoengineering of carbon-based electrodes to incorporate a high density of edges (such as from aligned GNRs,[30] graphene quantum dots,[54] or even large-scale vacancy defects[55]) could greatly benefit supercapacitors and deserves ample investigation.

Throughout this assessment, we also contemplated the impact of several factors that were outside the scope of this work but may be of interest in future research. For instance, it would be interesting to explore the influence of different edge-passivating functional groups on both the electronic structure and the EDL microstructure. In particular, the edge-induced perturbations to the EDL microstructure may be sensitive to the configuration and size of the functional group as well as the relative strength of electrostatic interactions with the constituent atoms. Here, we should also note that more strict quantitative predictions using our method may require additional considerations. For example, we did not model charge polarization at the electrode−electrolyte interface for simplicity, which may affect the EDL microstructure as well as the electronic structure of the electrode. In addition, conventional DFT can introduce self-interaction errors which may underestimate charge localization but can be mitigated using hybrid functional methods.[56] We also neglected charge transfer between [BMIM][PF$_6$] and the electrode since it appears to be unlikely.[57] Nevertheless, our computational approach is sufficient to demonstrate that the presence of edges can enhance the performance of supercapacitors by virtue of increasing both C_Q and C_D.

Table 1. Summary of Predicted Capacitances for Charged OH-18ZGNR Electrodes in [BMIM][PF$_6$][a]

σ (C g^{-1})	C_Q (F g^{-1})	C_D (F g^{-1})	C_T (F g^{-1})	ϕ_E (V)	ϕ_D (V)	ϕ_a (V)
+80.4	378.1 (134.7)	101.8 (55.4)	80.2 (39.3)	0.21	0.79	1.00
−80.4	300.6 (138.5)	103.1 (58.3)	76.8 (41.0)	−0.26	−0.78	−1.04

[a]For comparison, the capacitance values for the pristine graphene case are also shown in parentheses.

■ CONCLUSION

We investigated the impact of ZGNRs in $[BMIM][PF_6]$ ionic liquid on the quantum and EDL capacitances (and, therefore, the interfacial capacitance) using a combined DFT and classical MD approach. In our electronic structure analysis, we considered two different widths of H-passivated (H-18ZGNR and H-60ZGNR) and alternatingly H-/OH-passivated ZGNR (OH-18ZGNR/OH-60ZGNR) electrodes. Our results demonstrate that the electronic states are quasi-localized in the vicinity of the edges, although the degree of localization tends to decrease with increasing width. We then calculated the quantum capacitances (C_Q) from the electronic density of states. Comparisons with that of pristine graphene reveal that the ZGNR electrodes have significantly larger C_Q which are further enhanced as the ZGNR width decreases. Furthermore, our results show that the degree of excess charge accumulation at the edges increases superlinearly as the ZGNR width decreases. We also studied the influence of edge defects on the EDL microstructure using the OH-18ZGNR as a model system when the excess surface charge density $\sigma = 0$ and ± 80.4 C g^{-1}. We find that the presence of edges induces an alternating cascade of PF_6 and BMIM ions in which the segregation is greatest near the edges. Upon charging, the microstructure of the EDL exhibits a greater response near the edges due to the preferential accumulation of excess charge carriers toward the edges. As a result, the EDL capacitance (C_D) of the OH-18ZGNR case is also predicted to be greatly enhanced when compared to the pristine graphene case. Finally, the total interfacial capacitance ($C_T = [1/C_D + 1/C_Q]^{-1}$) of the OH-18ZGNR case is found to experience a 2-fold increase in comparison to the pristine graphene case when $\sigma = 80.4$ (-80.4) C g^{-1}. Our findings clearly highlight that the inclusion of a large density of edge defects in graphene-like electrodes can dramatically improve both C_Q and C_D and therefore the overall performance of supercapacitors.

■ ASSOCIATED CONTENT

Ⓢ Supporting Information

The DOS at varying vacuum spacing, calculated Bader charges at the edge of OH-18ZGNR, a molecular snapshot of the electrode−electrolyte interface, and additional details on the method to solve Poisson's equation. This material is available free of charge via the Internet at http://pubs.acs.org.

■ AUTHOR INFORMATION

Corresponding Author
*E-mail gshwang@che.utexas.edu; Ph 512-471-4847 (G.S.H.).
Notes
The authors declare no competing financial interest.

■ ACKNOWLEDGMENTS

■ REFERENCES

(1) Ribeiro, P.; Johnson, B.; Crow, M.; Arsoy, A.; Liu, Y. Energy Storage Systems for Advanced Power Applications. *Proc. IEEE* **2001**, *89*, 1744−1756.

(2) Hadjipaschalis, I.; Poullikkas, A.; Efthimiou, V. Overview of Current and Future Energy Storage Technologies for Electric Power Applications. *Renewable Sustainable Energy Rev.* **2009**, *13*, 1513−1522.

(3) Simon, P.; Gogotsi, Y. Capacitive Energy Storage in Nanostructured Carbon-Electrolyte Systems. *Acc. Chem. Res.* **2012**, *46*, 1094−1103.

(4) Wang, G.; Zhang, L.; Zhang, J. A Review of Electrode Materials for Electrochemical Supercapacitors. *Chem. Soc. Rev.* **2012**, *41*, 797−828.

(5) Chen, J.; Li, C.; Shi, G. Graphene Materials for Electrochemical Capacitors. *J. Phys. Chem. Lett.* **2013**, *4*, 1244−1253.

(6) El-Kady, M. F.; Strong, V.; Dubin, S.; Kaner, R. B. Laser Scribing of High-Performance and Flexible Graphene-Based Electrochemical Capacitors. *Science* **2012**, *335*, 1326−1330.

(7) Le, L. T.; Ervin, M. H.; Qiu, H.; Fuchs, B. E.; Lee, W. Y. Graphene Supercapacitor Electrodes Fabricated by Inkjet Printing and Thermal Reduction of Graphene Oxide. *Electrochem. Commun.* **2011**, *13*, 355−358.

(8) Guo, C. X.; Li, C. M. A Self-Assembled Hierarchical Nanostructure Comprising Carbon Spheres and Graphene Nanosheets for Enhanced Supercapacitor Performance. *Energy Environ. Sci.* **2011**, *4*, 4504−4507.

(9) Yang, X.; Cheng, C.; Wang, Y.; Qiu, L.; Li, D. Liquid-Mediated Dense Integration of Graphene Materials for Compact Capacitive Energy Storage. *Science* **2013**, *341*, 534−537.

(10) Yoo, J. J.; Balakrishnan, K.; Huang, J.; Meunier, V.; Sumpter, B. G.; Srivastava, A.; Conway, M.; Reddy, A. L. M.; Yu, J.; Vajtai, R.; et al. Ultrathin Planar Graphene Supercapacitors. *Nano Lett.* **2011**, *11*, 1423−1427.

(11) Choi, B. G.; Hong, J.; Hong, W. H.; Hammond, P. T.; Park, H. Facilitated Ion Transport in All-Solid-State Flexible Supercapacitors. *ACS Nano* **2011**, *5*, 7205−7213.

(12) Qiu, Y.; Zhang, X.; Yang, S. High Performance Supercapacitors Based on Highly Conductive Nitrogen-Doped Graphene Sheets SI. *Phys. Chem. Chem. Phys.* **2011**, *13*, 1−10.

(13) Jeong, H. M.; Lee, J. W.; Shin, W. H.; Choi, Y. J.; Shin, H. J.; Kang, J. K.; Choi, J. W. Nitrogen-Doped Graphene for High-Performance Ultracapacitors and the Importance of Nitrogen-Doped Sites at Basal Planes. *Nano Lett.* **2011**, *11*, 2472−2477.

(14) Jiang, B.; Tian, C.; Wang, L.; Sun, L.; Chen, C.; Nong, X.; Qiao, Y.; Fu, H. Highly Concentrated, Stable Nitrogen-Doped Graphene for Supercapacitors: Simultaneous Doping and Reduction. *Appl. Surf. Sci.* **2012**, *258*, 3438−3443.

(15) Sun, L.; Wang, L.; Tian, C.; Tan, T.; Xie, Y.; Shi, K.; Li, M.; Fu, H. Nitrogen-Doped Graphene with High Nitrogen Level via a One-Step Hydrothermal Reaction of Graphene Oxide with Urea for Superior Capacitive Energy Storage. *RSC Adv.* **2012**, *2*, 4498−4506.

(16) Xia, J.; Chen, F.; Li, J.; Tao, N. Measurement of the Quantum Capacitance of Graphene. *Nat. Nanotechnol.* **2009**, *4*, 505−509.

(17) Stoller, M. D.; Magnuson, C. W.; Zhu, Y.; Murali, S.; Suk, J. W.; Piner, R.; Ruoff, R. S. Interfacial Capacitance of Single Layer Graphene. *Energy Environ. Sci.* **2011**, *4*, 4685−4689.

(18) Paek, E.; Pak, A. J.; Hwang, G. S. A Computational Study of the Interfacial Structure and Capacitance of Graphene in $[BMIM][PF_6]$ Ionic Liquid. *J. Electrochem. Soc.* **2013**, *160*, A1−A10.

(19) Pak, A. J.; Paek, E.; Hwang, G. S. Tailoring the Performance of Graphene-Based Supercapacitors Using Topological Defects: A Theoretical Assessment. *Carbon* **2014**, *68*, 734−741.

(20) Pak, A. J.; Paek, E.; Hwang, G. S. Relative Contributions of Quantum and Double Layer Capacitance to the Supercapacitor Performance of Carbon Nanotubes in an Ionic Liquid. *Phys. Chem. Chem. Phys.* **2013**, *15*, 19741−19747.

(21) Paek, E.; Pak, A. J.; Hwang, G. S. Curvature Effects on the Interfacial Capacitance of Carbon Nanotubes in an Ionic Liquid. *J. Phys. Chem. C* **2013**, *117*, 23539−23546.

(22) Wood, B. C.; Ogitsu, T.; Otani, M.; Biener, J. First-Principles-Inspired Design Strategies for Graphene-Based Supercapacitor Electrodes. *J. Phys. Chem. C* **2014**, *118*, 4−15.

(23) Paek, E.; Pak, A. J.; Kweon, K. E.; Hwang, G. S. On the Origin of the Enhanced Supercapacitor Performance of Nitrogen-Doped Graphene. *J. Phys. Chem. C* **2013**, *117*, 5610−5616.

(24) Brownson, D. A. C.; Munro, L. J.; Kampouris, D. K.; Banks, C. E. Electrochemistry of Graphene: Not Such a Beneficial Electrode Material? *RSC Adv.* **2011**, *1*, 978−988.

(25) Song, W.; Ji, X.; Deng, W.; Chen, Q.; Shen, C.; Banks, C. E. Graphene Ultracapacitors: Structural Impacts. *Phys. Chem. Chem. Phys.* **2013**, *15*, 4799−4803.

(26) Banerjee, S.; Shim, J.; Rivera, J.; Jin, X.; Estrada, D.; Solovyeva, V.; You, X.; Pak, J.; Pop, E.; Aluru, N.; et al. Electrochemistry at the Edge of a Single Graphene Layer in a Nanopore. *ACS Nano* **2013**, *7*, 834−843.

(27) Vatamanu, J.; Cao, L.; Borodin, O. On the Influence of Surface Topography on the Electric Double Layer Structure and Differential Capacitance of Graphite/Ionic Liquid Interfaces. *J. Phys. Chem. Lett.* **2011**, *2*, 2267−2272.

(28) Xing, L.; Vatamanu, J.; Smith, G. D.; Bedrov, D. Nanopatterning of Electrode Surfaces as a Potential Route to Improve the Energy Density of Electric Double-Layer Capacitors: Insight from Molecular Simulations. *J. Phys. Chem. Lett.* **2012**, *3*, 1124−1129.

(29) Jia, X.; Campos-Delgado, J.; Terrones, M.; Meunier, V.; Dresselhaus, M. S. Graphene Edges: A Review of Their Fabrication and Characterization. *Nanoscale* **2011**, *3*, 86−95.

(30) Zhang, C.; Peng, Z.; Lin, J.; Zhu, Y.; Ruan, G.; Hwang, C.-C.; Lu, W.; Hauge, R. H.; Tour, J. M. Splitting of a Vertical Multiwalled Carbon Nanotube Carpet to a Graphene Nanoribbon Carpet and Its Use in Supercapacitors. *ACS Nano* **2013**, *7*, 5151−5159.

(31) Rogers, R.; Seddon, K. Ionic Liquids–Solvents of the Future? *Science* **2003**, *302*, 792−793.

(32) Xu, W.; Angell, C. Solvent-Free Electrolytes with Aqueous Solution-like Conductivities. *Science* **2003**, *302*, 422−425.

(33) Perdew, J. P.; Wang, Y. Accurate and Simple Analytic Representation of the Electron-Gas Correlation Energy. *Phys. Rev. B* **1992**, *45*, 13244−13249.

(34) Kresse, G.; Furthmüller, J. Efficient Iterative Schemes for Ab Initio Total-Energy Calculations Using a Plane-Wave Basis Set. *Phys. Rev. B: Condens. Matter* **1996**, *54*, 11169−11186.

(35) Vosko, S. H.; Wilk, L.; Nusair, M. Accurate Spin-Dependent Electron Liquid Correlation Energies for Local Spin Density Calculations: A Critical Analysis. *Can. J. Phys.* **1980**, *58*, 1200−1211.

(36) Blöchl, P. Projector Augmented-Wave Method. *Phys. Rev. B* **1994**, *50*, 17953−17979.

(37) Hod, O.; Barone, V.; Peralta, J. E.; Scuseria, G. E. Enhanced Half-Metallicity in Edge-Oxidized Zigzag Graphene Nanoribbons. *Nano Lett.* **2007**, *7*, 2295−2299.

(38) Lee, G.; Cho, K. Electronic Structures of Zigzag Graphene Nanoribbons with Edge Hydrogenation and Oxidation. *Phys. Rev. B* **2009**, *79*, 165440.

(39) Monkhorst, H. J.; Pack, J. D. Special Points for Brillouin-Zone Integrations. *Phys. Rev. B* **1976**, *13*, 5188−5192.

(40) Henkelman, G.; Arnaldsson, A.; Jónsson, H. A Fast and Robust Algorithm for Bader Decomposition of Charge Density. *Comput. Mater. Sci.* **2006**, *36*, 354−360.

(41) Jorgensen, W. L.; Maxwell, D. S.; Tirado-rives, J. Development and Testing of the OPLS All-Atom Force Field on Conformational Energetics and Properties of Organic Liquids. *J. Am. Chem. Soc.* **1996**, *118*, 11225−11236.

(42) Kaminski, G.; Jorgensen, W. L. Performance of the AMBER94, MMFF94, and OPLS-AA Force Fields for Modeling Organic Liquids. *J. Phys. Chem.* **1996**, *100*, 18010−18013.

(43) Plimpton, S. Fast Parallel Algorithms for Short-Range Molecular Dynamics. *J. Comput. Phys.* **1995**, *117*, 1−19.

(44) Hoover, W. Canonical Dynamics: Equilibrium Phase-Space Distributions. *Phys. Rev. A* **1985**, *31*, 1695−1697.

(45) Son, Y.-W.; Cohen, M. L.; Louie, S. G. Energy Gaps in Graphene Nanoribbons. *Phys. Rev. Lett.* **2006**, *97*, 216803.

(46) Pisani, L.; Chan, J.; Montanari, B.; Harrison, N. Electronic Structure and Magnetic Properties of Graphitic Ribbons. *Phys. Rev. B* **2007**, *75*, 064418.

(47) Bovio, S.; Podesta, A.; Lenardi, C.; Milani, P.; Na, C. I. M. I.; Fisica, D. Evidence of Extended Solidlike Layering in [Bmim][NTf₂] Ionic Liquid Thin Films at. *J. Phys. Chem. B* **2009**, *113*, 6600−6603.

(48) Mezger, M.; Schröder, H.; Reichert, H.; Schramm, S.; Okasinski, J. S.; Schöder, S.; Honkimäki, V.; Deutsch, M.; Ocko, B. M.; Ralston, J.; et al. Molecular Layering of Fluorinated Ionic Liquids at a Charged Sapphire (0001) Surface. *Science* **2008**, *322*, 424−428.

(49) Maolin, S.; Fuchun, Z.; Guozhong, W.; Haiping, F.; Chunlei, W.; Shimou, C.; Yi, Z.; Jun, H. Ordering Layers of [bmim][PF₆] Ionic Liquid on Graphite Surfaces: Molecular Dynamics Simulation. *J. Chem. Phys.* **2008**, *128*, 134504.

(50) Kislenko, S. A.; Samoylov, I. S.; Amirov, R. H. Molecular Dynamics Simulation of the Electrochemical Interface between a Graphite Surface and the Ionic Liquid [BMIM][PF₆]. *Phys. Chem. Chem. Phys.* **2009**, *11*, 5584−5590.

(51) Feng, G.; Zhang, J. S.; Qiao, R. Microstructure and Capacitance of the Electrical Double Layers at the Interface of Ionic Liquids and Planar Electrodes. *J. Phys. Chem. C* **2009**, *113*, 4549−4559.

(52) Vatamanu, J.; Borodin, O.; Smith, G. D. Molecular Insights into the Potential and Temperature Dependences of the Differential Capacitance of a Room-Temperature Ionic Liquid at Graphite Electrodes. *J. Am. Chem. Soc.* **2010**, *132*, 14825−14833.

(53) Potential drop in the EDL and EDL capacitances are extrapolated from ref 18.

(54) Liu, W.; Yan, X.; Chen, J.; Feng, Y.; Xue, Q. Novel and High-Performance Asymmetric Micro-Supercapacitors Based on Graphene Quantum Dots and Polyaniline Nanofibers. *Nanoscale* **2013**, *5*, 6053−6062.

(55) Lin, Y.; Watson, K. A.; Kim, J.-W.; Baggett, D. W.; Working, D. C.; Connell, J. W. Bulk Preparation of Holey Graphene via Controlled Catalytic Oxidation. *Nanoscale* **2013**, *5*, 7814−7824.

(56) Cohen, A. J.; Mori-Sánchez, P.; Yang, W. Insights into Current Limitations of Density Functional Theory. *Science* **2008**, *321*, 792−794.

(57) Ghatee, M. H.; Moosavi, F. Physisorption of Hydrophobic and Hydrophilic 1-Alkyl-3-methylimidazolium Ionic Liquids on the Graphenes. *J. Phys. Chem. C* **2011**, *115*, 5626−5636.